Nanoscale

Accepted Manuscript

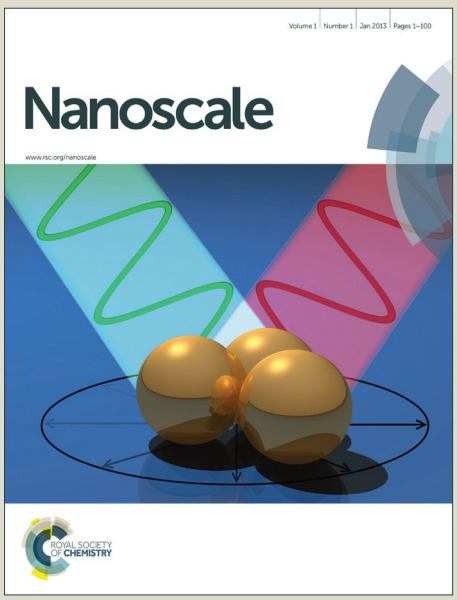

ROYAL SOCIETY OF CHEMISTRY

www.rsc.org/nanoscale

Effects of Crystallographic Facet-Specific Peptide Adsorption along Single ZnO Nanorods on the Characteristic Fluorescence Intensification on Nanorod Ends (*FINE*) Phenomenon

*Manpreet Singh†, Xiaolu Zhuo‡, Daniel S. Choi†, Lorelis E. Gonzalez†, Jianfang Wang‡, and Jong-in Hahm†**

†Department of Chemistry, Georgetown University, 37th & O Sts. NW., Washington, DC, 20057 USA.

‡Department of Physics, The Chinese University of Hong Kong, Shatin, Hong Kong SAR, CHINA.

**Address Correspondence to jh583@georgetown.edu*

ABSTRACT

The precise effect of crystallographically discriminating biomolecular adsorption on the fluorescence intensification profiles of individual zinc oxide nanorod (ZnO NR) platforms was elucidated in this study by employing peptide binding epitopes biased towards particular ZnO crystal surfaces and isolating the peptides on given crystalline facets of ZnO NRs. Subsequently, the fluorescence emission profiles of the preferentially bound peptide cases on the basal versus prismic planes of ZnO NRs were carefully evaluated both experimentally and via computer simulations. The phenomenon of fluorescence intensification on NR ends (*FINE*) was persistently observed on the individual ZnO NR platforms, regardless of the location of the bound peptides. In contrast to the consistent occurrence of *FINE*, the degree and magnitude of *FINE* were largely influenced by the discriminatory peptide adsorption to different ZnO NR facets. The temporal stability of the fluorescence signal was also greatly affected by the selectively located peptides on the ZnO NR crystal when spatially resolved on different NR facets. Similarities and differences in the spatial and temporal fluorescence signal of the crystalline NR facet-specific versus -nonspecific biomolecular adsorption events were then compared. To further illuminate the basis of our experimental findings, we also performed finite-difference-time-domain (FDTD) calculations and examined the different degrees of *FINE* by modelling the biased peptide adsorption cases. Our multifaceted efforts, providing combined insight into the spatial and temporal characteristics of the biomolecular fluorescence signal characteristically governed by the biomolecular location on the specific NR facets, will be valuable for novel applications and accurate signal interpretation of ZnO NR-based biosensors in many rapidly growing, highly miniaturized biodetection configurations.

INTRODUCTION

Optically superior materials of reduced dimensionality and subsequently fabricated optical devices configured in a miniaturized format have drawn considerable research interest in recent years,[1-4] demonstrating potentially useful applications in biosensing and biodetection through newly identified fundamental optical phenomena.[5-9] The excellent optical properties of zinc oxide (ZnO) have been widely recognized and extensively exploited as light emitting diodes,[10,11] field emitters,[12,13] lasers,[14-16] and waveguides[15,17-20] in optoelectronics. The optical characteristics of ZnO have also proven to be beneficial in the biosensing arena in later years, as evidenced by the much improved detection sensitivity of biomolecular fluorescence when paired with ZnO nanomaterials such as nanoparticles (NPs) and nanorods (NRs).[5-7,9,21-25]

Size reduction in ZnO-based biosensors and biodetection can aid in the practical needs for more portable, low-volume, minimally invasive, highly sensitive, and increased throughput bioassays. In addition, novel biodevice architectures can be designed to take advantage of the unique optical characteristics of individual ZnO nanomaterials that can be otherwise obscured in ensemble-averaged responses. Accordingly, it is likely the future integration of ZnO will involve not only the nanoscale form of the material, but also configure a single nanomaterial as a distinct detection component instead of a nanomaterial ensemble. To this end, we recently reported on the intriguing optical phenomenon of fluorescence intensification on NR ends (*FINE*) seen from fluorophore-coupled proteins adsorbed indiscriminately along a single ZnO NR.[26,27] We considered the influence of experimental parameters such as the growth orientation and physical dimensions of the ZnO NRs (material factors) as well as the type and concentration of the fluorophores (biomolecular factors) on the resulting biomolecular fluorescence profiles.

Convoluted contributions from the material and biomolecular factors evaluated in the previous work may still impose a limitation in the fundamental understanding and further biomedical application of the highly useful *FINE* effect pertaining to the spatially localized and temporally extended fluorescence intensification. Before the full potential of individual ZnO NRs in biodetection is realized, it is critical

to understand the precise effect of biomolecular fluorescence emitters bound on different crystalline facets of a ZnO NR on the resulting optical signal. Despite the prior investigations, the important study of controlling specific biomolecular adsorption behaviors on different ZnO crystal planes and pinpointing the roles of such adsorption scenarios on the subsequent signal enhancement and quantification has not been performed to date. Yet, such information can serve not only to facilitate accurate interpretations of the enhanced optical signal and the mechanism of ZnO NR-enabled *FINE* but also to promote the rational design of better nanoscale ZnO biomaterials and biosensors.

Peptides can serve as useful surrogates for whole proteins given their synthetic accessibility and recognition potential for different surfaces or biomolecules.[28,29] Distinctly located amino acid residues encoded within the peptide sequence can provide specific interactions with strong binding affinities for target receptors or materials that may not otherwise be conveniently achieved with small molecules or larger proteins. Given the modular nature of peptides, it is further possible to employ combinatorial methods to rationally design short sequences with high affinity for specific surfaces. Accordingly, we turn to peptide binding epitopes biased towards particular ZnO crystal surfaces to address the need for controlled biomolecular adsorption. A series of peptide binding epitopes was previously identified via spectroscopic means and further used to promote solution-processed ZnO growth along a predefined axis into a controlled shape.[30-34]

We exploit such amino acid sequence-specific peptide interactions with given ZnO crystal facets[30,33] in this study to yield discriminating adsorption cases in which the adsorption of fluorophore-coupled biomolecules is localized either to the basal or prismic planes of the ZnO NRs. We subsequently examine the fluorescence emission profiles of the preferentially bound peptide fragments both spatially along the NR long axis and temporally from different NR facets under constant irradiation. Spatially, we probe the optical signal from the end and main body of the NR distinctively to examine for the occurrence of the highly localized optical phenomenon of *FINE* and further elucidate the role by which facet-discriminating adsorption of the biomolecules affects the degree of signal enhancement in *FINE* for NRs of different physical dimensions. We also monitor the resulting emission temporally to probe

the fluorescence decay profile of each peptide case along the length of the individual ZnO NRs. We further identify similarities and differences in the spatial and temporal fluorescence signal between the crystalline NR facet-specific versus -nonspecific biomolecular adsorption events. In addition, we perform finite-difference-time-domain (FDTD) calculations to compare the ensuing simulation results with the experimental outcomes and to further illuminate the basis of our experimental findings.

The key findings of our combined experimental and simulation investigation are multifold. The presence of *FINE* is consistently observed on the individual ZnO NR platforms regardless of the location of the bound peptides. From both basal and prismic facet-bound peptide cases, fluorescence signal is continuously monitored on all positions of the NR, not just on the peptide adsorption planes. On the contrary, discriminatory peptide adsorption to different ZnO NR facets affects the degree and intensity of *FINE*. The fluorescence intensity and its temporal emission stability are revealed to be higher for the peptide fragments adsorbed on the NR prismic plane. In addition, the dependence of the degree of *FINE* on the NR length is found to be much stronger for the peptides preferentially adsorbed on the prismic plane than on the basal plane. The FDTD simulations further corroborate our experimental findings and provide a fundamental basis for the discussion of the contributing factors leading to the *FINE* phenomenon.

A better understanding of the manifestation of *FINE* is anticipated to support the signal processing and interpretation of already demonstrated ZnO NR biodevices and to encourage the exploration of novel applications exploiting the highly directional and locally enhanced optical signal. In this regard, our efforts will be highly valuable to the growing use of individual ZnO nanomaterials in fabricating high sensitivity sensors. By decoupling the biomolecular factors, such as the location and amount of biomolecules, from the nanomaterial factors, such as the inherent ZnO optical properties and the high shape anisotropy of the NR, our efforts will also deepen the understanding of the complex pathways of signal intensification on the ZnO NR ends with important relevance to optical biomedical assays.

EXPERIMENTAL SECTION

The controllable synthesis of ZnO NRs was performed via chemical vapor deposition in a customized horizontal tube furnace. The feedstock source, a 2:1 by weight mixture of zinc oxide (99.999% purity) and graphite (99.99% purity) powders obtained from Alfa Aesar Inc., was placed in a quartz source boat and positioned on top of the heating source located at the center of the tube furnace. The target quartz boat containing the growth substrate, a 1 x 1 cm^2 Si wafer (0.432 mm thickness) received from Silicon Quest, Inc (San Jose, CA), was placed 15.6 cm away from the source materials, downstream from the Ar carrier gas flow. To mediate the heteroepitaxial growth of ZnO NRs on Si, the Si wafer was pretreated with 20 μL of a growth catalyst, 20 nm Au colloid from Ted Pella, Inc. (Redding, CA), for 5 min. Subsequent carbothermal reduction of the feedstock source was achieved by heating the furnace to 950 °C for 20 min to 1 h at a ramp-up/ramp-down rate of 15 °C min^{-1} under a constant Ar gas flow of 100 standard cubic centimeters per minute for growth of vertically oriented ZnO NRs. Slight alterations to the growth time and distance between source and target boats allowed for growth of NRs with varying aspect ratios. The sample was then retrieved for structural characterization using a FEI/Phillips XL 20 scanning electron microscope (SEM) operating at 20 kV. The as-grown ZnO NRs were then dispersed into ethanol via ultrasonication and deposited onto a pre-cleaned 1x1 cm^2 Si wafer for subsequent biomolecular detection.

For biomolecular treatment of the ZnO NR platform, custom-synthesized peptide fragments of PT32 and PT44 with the specific amino acid sequence of HVSIHRTTHHEM and HSSHHQPKGTNP, respectively, were received from GenScript Inc. (Piscataway, NJ). The molecular weight and the isoelectric point of the peptide pieces are 1987.19 Da (1828.92 Da) and 7.10 (8.77) for PT32 (PT44). The fragments were pre-conjugated with fluorescein isothiocyanate-aminohexanoic acid (FITC-Ahx) at the N-terminus. The as-received peptides were reconstituted in deionized water (DI) per manufacturing recommendations. The ZnO NRs were incubated with 20 μL of varying concentrations of each peptide for 5 min in a humidity-controlled chamber protected from light. Post-incubation, the ZnO NR sample was washed thoroughly with DI, gently dried using N_2, and immediately imaged.

All optical measurements were carried out using a Zeiss Axio Imager A2M (Carl Zeiss, Inc., Thornwood, NY) microscope equipped with an AxioCAM HRm digital camera. Reflected bright-field illumination and unpolarized fluorescence excitation were produced using a 12V/100 W halogen lamp and a 120 W mercury vapor lamp (X-Cite 120Q), respectively. To ensure the collected signal is resultant from only the biomolecular fluorescence of the peptides, a dichromatic beam splitter was employed to separate the 450-490 nm excitation from the 510-540 nm collection of the biomolecular emission. All images were acquired using an EC Epiplan-NEOFLUAR 50x magnification (Numerical Aperture, NA = 0.8) objective lens. For the photobleaching experiments, the sample was constantly irradiated for 10 min with periodic imaging using a 2 sec exposure in a dark room to obtain time-lapse images. The image analysis was subsequently performed using AxioVision (Carl Zeiss, Inc.), Image J (a Java-based image processing program), and Origin 8 (OriginLab Corp.) software.

All simulations were conducted using FDTD Solution 8.7 developed by Lumerical Solutions, Inc. In the simulations, the ZnO NR was modeled as a hexagonal prism with a diameter of 100 nm of varying length. The refractive index of ZnO was taken to be 2.04,[35] while the surrounding medium was set to 1. An electric dipole with radiation wavelength of 517 nm was placed 2 nm away from the NR surface to best represent the spectroscopic and spatial condition of the fluorophore-coupled biomolecules used in the experiments. We considered the dipole direction that enables the most effective radiation coupling of the emitter to the NR, whose setting corresponds to the dipole polarization perpendicular to the ZnO NR surface. To simulate for the discrimination of each peptide toward the different facets of the NR, the electric dipole was accordingly positioned either at the NR main body (prismic plane) or end (basal plane) for the case of PT32 and PT44, respectively. A non-uniform mesh was employed for the best tradeoff between the simulation accuracy, speed, and memory requirements. In vicinity of the electric dipole, the nanostructure and its surrounding medium were divided into meshes of 1 nm in size. For the other areas, a coarse mesh up to 5 nm was employed.

RESULTS AND DISCUSSION

ZnO NR Crystal Facet-Specific Peptide Adsorption. A representative SEM image of the typical ZnO NR platform employed in our peptide adsorption studies is provided in Fig. 1(A) with a corresponding colored schematic in the right panel to illustrate the different low-index crystal planes of the polar {0001} and nonpolar $\{10\bar{1}0\}$ facets on the exposed surface of the wurtzite ZnO NR. The highly crystalline ZnO NR exposes six prismic planes along the NR side facets and two basal planes at the NR end facets. For discriminatory adsorption onto the basal versus prismic planes of ZnO NRs, we exploit two short peptide sequences that have shown clear adsorption bias either to the family of basal or prismic facets on the exposed surface of the wurtzite ZnO NR.[30,31] In recent years, phage-display experiments have become a reliable technique by which to screen large pools of peptides to probe their affinity for optically interesting inorganic materials such as noble metals, semiconductors and metal oxides.[30,34] Using this approach, a strong ZnO binding peptide referred to as PT44, with the amino acid sequence of HSSHHQPKGTNP, was identified to exhibit high specificity for binding onto the basal planes of ZnO {0001}.[30] In addition, a contrasting peptide named PT32, with the sequence of HVSIHRTTHHEM, was reported to show a high binding affinity for the prismic planes of ZnO $\{10\bar{1}0\}$.[31] In the top panel of Fig. 1(B), a magnified SEM image reveals the well-defined, rectangular prismic plane comprising the ZnO NR side facet that serves as the preferential binding site for the PT32 biomolecules. The zoomed-in SEM view of Fig. 1(C) clearly shows the hexagonal basal plane at the ZnO NR end facet that provides the highly favored adsorption site for the PT44 fragments. The discriminating binding preferences of the FITC-Ahx-labeled PT32 and PT44 biomolecules toward the different ZnO NR crystal planes are schematically depicted below each SEM image in Fig. 1 (B and C). In the bottommost panels of Fig. 1, the ball and stick model of the amino acids encoding the high-affinity interaction of each 12-mer peptide of PT32 and PT44 for its respective crystal plane are also illustrated without the N-terminal FITC-Ahx modification.

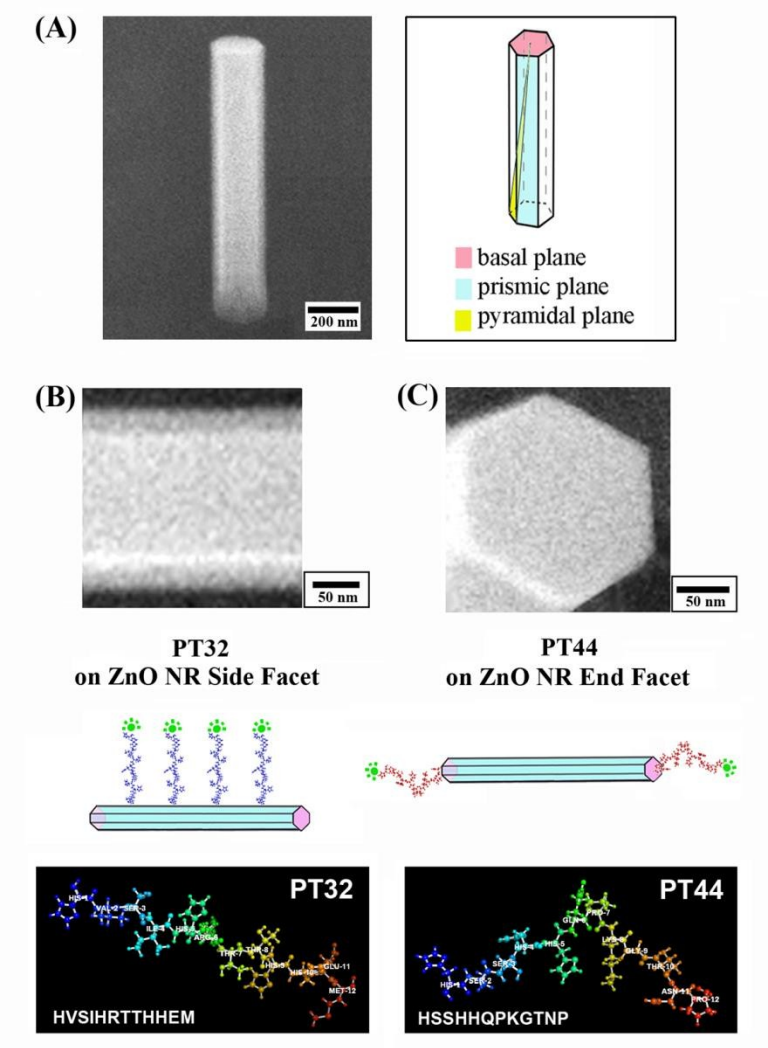

Figure 1. (A) A SEM image of a typical ZnO NR showing the basal (NR end) and the prismic (NR side) facets. The different crystal planes exposed on the ZnO NR are defined in the colored schematic on the right. **(B)** The zoomed-in SEM view of the rectangular side facet along the main body of the NR depicts the ZnO crystal plane that serves as the preferential binding sites for the PT32 fragments. **(C)** The hexagonal NR end facet highly favored for the adsorption of the PT44 strands is clearly shown in the magnified SEM image. In the bottom panels of (B) and (C), schematics depicting the discriminatory biomolecular adsorption behaviors on different ZnO NR facets are shown along with ball and stick models of each peptide.

Influence of Facet-Specific Adsorption on the Intensity and Degree of Biomolecular Fluorescence. The ability of PT32 and PT44 to discriminate between the basal and prismic crystallographic planes allows for a unique opportunity to probe the potential role of facet selective biomolecular adsorption on the intensity and degree of enhanced fluorescence signal. To substantiate the role by which facet-selective adsorption affects the biomolecular fluorescence signal measured along individual NRs and the optical phenomenon of ZnO NR-enabled *FINE*, individual NR platforms were incubated with 25 μg/mL of either fluorophore-conjugated peptide, PT32 or PT44. The subsequent biomolecular emission was systematically probed and the intensity of the resulting optical signal was monitored both spatially, as a function of the position along the NR length, and temporally, as function of time under constant irradiation. Further, the occurrence, degree, and photostability of *FINE* were examined as a function of the position along the NR and the physical dimensions of the NR for each crystallographically favored peptide adsorption case. For the systematic profiling of biomolecular emission, over 200 ZnO NRs showing a range of size distributions were evaluated for the manifestation of *FINE* to unambiguously determine the influence of different facet-bound peptide cases on the magnitude and degree of *FINE*.

Fluorescence Profiled Spatially and Temporally for PT32 and PT44 on Individual ZnO NRs. The three-dimensional (3D) contour plots in Fig. 2 display the time-dependent decay of fluorescence intensity under constant irradiation at each position along the length of individual ZnO NRs. Characteristic biomolecular emission profiles of PT32 and PT44 are displayed in Fig. 2(A and B), respectively, for ZnO NRs of various lengths. In our previous investigation, we showed that the degree of *FINE* is dependent on the length of the NR with longer NRs showing increased levels of *FINE* whereas NR width does not play a significant role.[26] Hence, we tested the effect of the crystallographically specific peptide adsorption on the spatial and temporal fluorescence signal by employing ZnO NRs of different lengths.

When comparing the biomolecular fluorescence profiles monitored along the long axis of the NRs for the two cases of PT32 and PT44, we note several interesting outcomes which may be valuable in further

providing insight into the origin of *FINE*. Firstly, fluorescence signal was present on all positions of the ZnO NRs for both PT32 and PT44, regardless of each peptide's intrinsic adsorption affinity for binding to either the NR side or end facets. For instance, fluorescence signal was clearly resolved not only along the NR main body but also from the NR end positions for the PT32 case. Similarly, the signal for the PT44 case was present not only on the end facets but also on the NR main body. This interesting observation of biomolecular fluorescence signal which is present continuously along all NR positions including the ZnO NR positions away from the favored peptide binding sites indicates that the observed signal is not directly correlated with the spatial distribution of adsorbed peptides on the NRs. The resulting optical signal is rather related to the collectively guided signal of the biomolecular fluorescence through the optical 1D channels of ZnO NRs. This observation may further be explained by the electromagnetic radiation, upon its initial coupling of biomolecular emission into the NR medium, which propagates along the length of the ZnO NR in the form of surface evanescent waves and guided waves and finally radiates out to the far field from the NR ends. Secondly, the highly localized intensification of fluorescence signal from the NR ends relative to that from the main body is clearly evidenced for the two peptide cases, once again irrespective of the peptide's specific binding preference. Since the manifestation of *FINE* is seen even for the cases of PT32, in which the biomolecules preferentially adsorb along the NR main body, the origin of the enhanced signal localized at the NR end facets cannot be simply explained by the potential circumstance of exclusive or increased biomolecular adsorption at the NR ends relative to the main body.

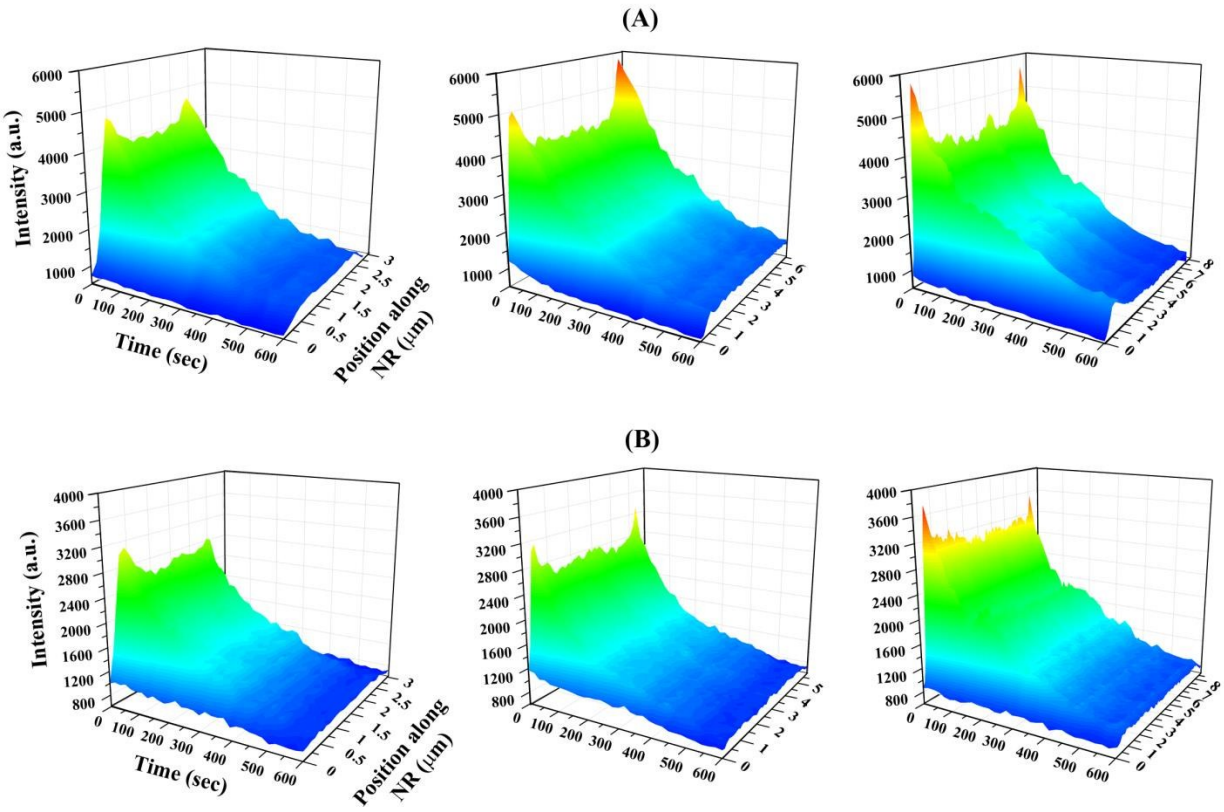

Figure 2. 3D contour plots of the fluorescence intensity profile collected from **(A)** PT32 and **(B)** PT44 preferentially adsorbed onto the side and end facets of the individual NRs, respectively. From left to right, the three panels of the contour plots selected for the two PT sequences in (A) and (B) display the typical PT fluorescence intensity on NRs of increasing rod lengths as a function of position on the NR as well as time under constant illumination.

Measured Fluorescence Intensity Along the NR for PT32 versus PT44. For the case of PT32, as the NR lengths change from shorter to longer from the left to the right panels of Fig. 2(A), the biomolecular fluorescence intensity along the NR main body remains steady at a constant intensity value of approximately 4000 arbitrary unit (a.u.). Such results are expected at constant peptide concentration because the density of PT32 fragments on the NR side facet (the adsorbed peptides per given area of the NR side facet) does not change along the NR main body, even though there is an increase in the surface area of the NR side facet as a result of the longer lengths providing additional binding sites for PT32 on the NR main body. The intensity measured on the NR end facets for PT32, however, becomes

progressively higher with the increase in NR length. This observation of higher fluorescence intensity measured at the NR end positions with longer NR lengths is highly unexpected from the NR side facet-favoring PT32 and is in stark contrast to the relatively constant signal along the NR main body seen with increasing NR lengths. As prismic facets on the NR main body dominate the exposed surface area of the ZnO NR, the rising fluorescence intensity at the NR end position for longer NRs cannot be derived from high amounts of fluorophore-conjugated peptides positioned at the NR end facets due to the prismic facet-selective PT32. As indicated previously, the enhanced signal measured at the NR end positions is likely to have collective signal contributions from the PT32 biomolecules adsorbed along the NR main body which can effectively couple their emission through the underlying optical medium of the ZnO NR for subsequent guided propagation to the NR ends. As increases in NR length allow for greater amounts of adsorbed PT32 fragments along the main body, higher levels of emitted fluorescence may couple into the ZnO NR and further be collectively guided to the NR ends, leading to fluorescence intensity and, in addition, higher degrees of signal intensification at the NR ends for elongated NRs.

For the case of PT44, as NR length increases from the left to right panels of Fig. 2(B), the signal monitored along the NR main body was approximately 30% lower in fluorescence intensity than that found for PT32. In fact, the overall intensity observed at any position along the length of the ZnO NRs was found to be higher for the PT32 than the PT44 case. The typical diameter range of the employed ZnO NRs in our experiment is between 100 and 350 nm, and the majority of these ZnO NRs exhibit an aspect ratio greater than 10:1 in length:width which is equivalent to a ratio of 30:1 (NR side facet: NR end facet) in terms of the total surface area availabe for peptide binding. Since PT44 has a binding predilection for the basal planes, which provide a much smaller and relatively constant surface footprint for biomolecular adsorption relative to PT32, it can be reasoned that neither the increase in NR physical size nor in biomolecular concentration will have a major influence on the fluorescence intensity. Indeed for PT44, only very small increases in fluorescence intensity were measured on the NR end facets with longer NR lengths. The intensities measured on the NR end facets for PT44 have a very weak dependence on the NR length when compared to the PT32 case, and NR widths do not have a noticeable

effect on the observed fluorescence intensity. We also observe that the intensity values monitored along the NR main body appear to show a slightly increasing trend with longer NRs. These experimental outcomes will be discussed further with the aid of the FDTD simulations presented later in this paper.

The large number of ZnO NRs employed to verify the aforementioned trends in the presence and degree of *FINE* allows us to rule out any influences arising from potentially uneven spatial distributions of the excitation light intensity. The biomolecular emission profiles characterized along the NR long axis and subsequently compared between the PT adsorption cases in this study were indeed confirmed from over 200 NRs, regardless of NR location on the sample plane. Although different NRs under the same illumination spot, i.e. NRs subject to potentially varying excitation intensity along the NR length, were examined for their *FINE* characteristics, the PT32 and PT44 adsorption-specific trends in biomolecular fluorescence intensity and signal distribution along the NR length were consistently observed.

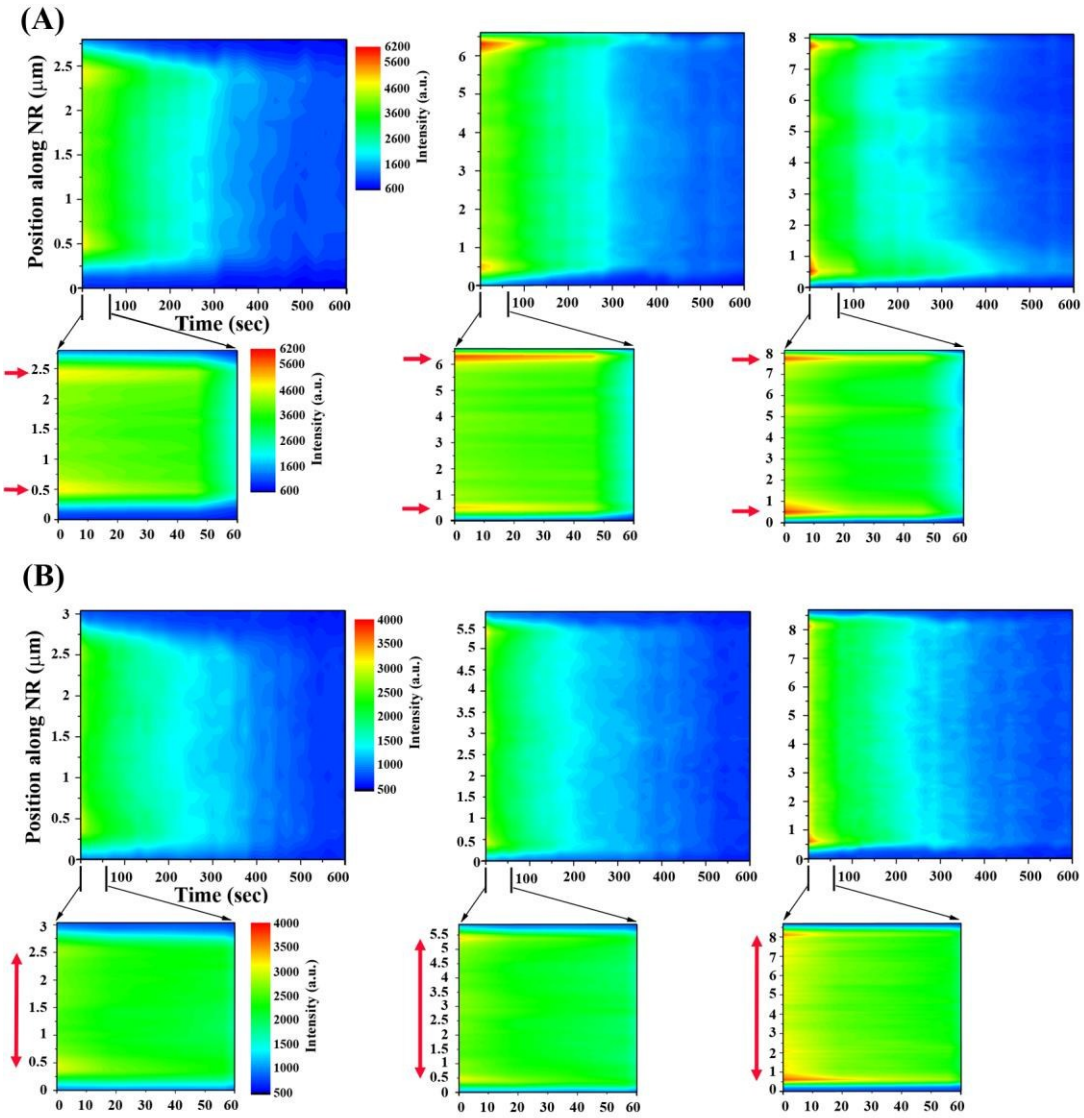

Figure 3. 2D surface plots of the fluorescence intensity profile collected from **(A)** PT32 and **(B)** PT44 preferentially adsorbed onto the side and end facets of the individual NRs, respectively. The photoactivated fluorescence decay profile of PT32 and PT44 on ZnO NRs and their respective degrees of *FINE* are better identified in the early time graph shown below each main panel for qualitative comparison. The different extents to which spatial localization and delocalization of the intensified fluorescence signal along each position of the NRs measured in the case of PT32 and PT44, respectively, are indicated as the two red arrows in the zoomed-in panels. Two distinctive arrows inserted in each early time panel in **(A)** mark the two NR end regions with highly localized intense signal measured to be greater than 80% of the maximum fluorescence intensity. The double-headed

arrows in early time panels in **(B)** denote all the NR positions which exhibit intensities larger than 80% of the highest fluorescence intensity seen.

Spatial Localization Profile of Fluorescence for PT32 versus PT44. In order to present clearly the spatial distribution of the fluorescence intensity at various positions on the individual NRs as well as the time-dependent decay profile under constant illumination, two-dimensional (2D) surface plots profiling the characteristic intensification of fluorescence on the NR ends relative to the main body are provided for PT32 and PT44 preferentially adsorbed onto the NR side and end facets in Fig. 3(A and B), respectively. For each peptide, results from NRs of increasing lengths are displayed with the early time graphs below each panel, providing clearer views of the photoactivated fluorescence decay profile of PT32 and PT44 as well as their respective degrees of *FINE*. The intensification of fluorescence at the NR ends can be seen for all cases but generally persists longer over time with a higher degree of enhancement for PT32 relative to PT44. The spatial distributions of the measured fluorescence signals along the long axis of the NRs in the 2D panels in Fig. 3 clearly indicate that the spatial localization of the enhanced fluorescence signal on the NR ends is highly pronounced for the PT32 case relative to PT44. When comparing the fluorescence signal intensity measured at the NR end facets for the PT32 (A) and PT44 (B) cases using the zoomed-in views of the right-most early-time fluorescence panels, two specific NR positions corresponding to the two end positions of the NR are identified as high intensity positions for the PT32 sample. In contrast, while the NR ends are still identified as the regions of the highest intensity for the PT44 sample, a considerable amount of persisting intensity is seen throughout the length of the NR. This relative delocalization of the fluorescence signal in PT44 compared to PT32 can be found in the early time 2D panels in which the magnitude of signal reaching approximately 80% of the highest intensity measured at the NR ends is persistently and continuously shown for PT44. For the PT32 samples, on the other hand, the signal intensity quickly drops to 50% of the highest magnitude

measured at the NR ends even for a short distance away from the end positions, leaving the intensified fluorescence signal highly spatially localized at the NR ends.

We were able to elucidate the similarities and differences between NR facet-discriminating versus nondiscriminating biomolecular adsorption cases by comparing the results between this and our earlier study. In all biomolecular adsorption cases on ZnO NRs, the fluorescence signal is observed from all positions on the NR regardless of the physical locations of the biomolecules. The occurrence of *FINE* is also confirmed in all cases. The new outcomes from the crystallographic plane-specific adsorption cases further reveal that the biomolecules adsorbed on the NR main body, relative to those on the NR end facets, will contribute much more strongly to the overall signal intensity regardless of whether it is measured on the NR side or end facets. Our new findings from the facet-specific study also reveal that the NR length-dependence on the degree of *FINE* is much more pronounced for the biomolecules adsorbed on the NR main body, whereas the correlation between the degree of *FINE* and the NR length is found to be weak for the biomolecules bound on the NR end facets.

Influence of Facet-Specific Adsorption on the Temporal Stability of Biomolecular Fluorescence. To further probe the temporal stability of the fluorescence signal monitored along the various positions of individual ZnO NRs for the two peptide binding cases, the exponential decay of the emission under constant irradiation is quantitatively profiled in Fig. 4 for the NRs of different lengths. The typical photostability curves of PT32 and PT44 are respectively presented in Fig. 4(A and B) for NRs of 2.5 μm (left), 5.5 μm (center), and 7.5 μm (right) in length. The signal intensity for each peptide and NR length panel was normalized with respect to the highest and lowest intensities measured initially at T = 0 s. To evaluate the temporal stability of the biomolecular emission, we define $T_{1/2}$, $T_{1/5}$, and $T_{1/10}$ as the time taken for the collected signal to decrease to 50%, 20%, and 10% of the initial intensity at T = 0 s.

When comparing the stability profiles of each peptide, PT32 generally exhibited extended photostability at each time point relative to PT44. The prolonged temporal stability of PT32

fluorescence can be seen by comparing the $T_{1/2}$, $T_{1/5}$, and $T_{1/10}$ values of PT32 (98 s, 226 s, and 320 s) with those of PT44 (59 s, 191 s, and 330 s) for the 2.5 μm NR case. This effect can be also found when viewing the early time, 2D graphs in Fig. 3. The enhanced signal at the NR ends is consistently observed to be prolonged for PT32 versus PT44 both in the 2D plots in Fig. 3 and in the photostability graphs in Fig. 4. These outcomes combinedly suggest that the signal from each emitter adsorbed on the ZnO main body for the PT32 case results in temporally protracted propagation of light through waveguiding of the signal along the ZnO NR optical medium once fluorescence is channeled into the NR. For PT44, the contribution from NR-mediated light guiding will be relatively lower since the fluorescence emitters are already placed on the basal planes from which the radiation into the far field may effectively occur.

When considering all three NRs of different lengths, the average $T_{1/2}$, $T_{1/5}$, and $T_{1/10}$ values as a result of PT32 fluorescence are measured to be 93 s, 230 s, and 333 s, respectively. Those time points marking $T_{1/2}$, $T_{1/5}$, and $T_{1/10}$ for the PT44 case are 65 s, 193 s, and 314 s, instead. The temporal stability of the resulting emission collected from the NR side and end facets showed similar decay profiles for each peptide case, irrespective of the intrinsic preference of PT32 and PT44 to selectively adsorb onto the NR side or end planes, respectively. The comparable PT fluorescence decay profiles over time observed on the NR end and side facets are different than the outcomes from our previous investigations.[26,27] In those earlier studies, fluorophore-tagged proteins were adsorbed onto all exposed NR facets with no facet-specific binding bias, which enabled temporally prolonged observation of the biomolecular fluorescence on the NR ends relative to the NR side facets. This difference in temporal stability on the NR end versus side facets between the crystallographic plane-specific and nonspecific cases may be due to the unique situation of PT adsorption yielding no signal emitters on the non-binding facets. Rather than the dual sources for the measured signal contributed from biomolecules on both basal and prismic planes in the non-biased binding case, the time-dependent intensity decay profile for the facet-discriminatory PT adsorption case will be affected by only a single source, i.e. the PTs adsorbed on either the basal or prismic planes. In this latter case, time-dependent fluorescence decay

profiles are expected to have similar contributions to different NR positions along the length as they are all guided from the same source.

Apart from these differences in temporal stability identified between the NR facet-specific versus nonspecific adsorption events, a similarity of generally extended photostability is found on all the biomolecular adsorption cases on ZnO NRs we investigated. When considering the fact that most organic fluorophores showing molar extinction coefficients of 5-10 x 10^4/(M•cm) typically exhibit $T_{1/2}$ values shorter than 15 s,[36-39] the use of a ZnO NR platform extends the photostability of biomolecular fluorophores considerably regardless of the NR plane selectivity in biomolecular adsorption.

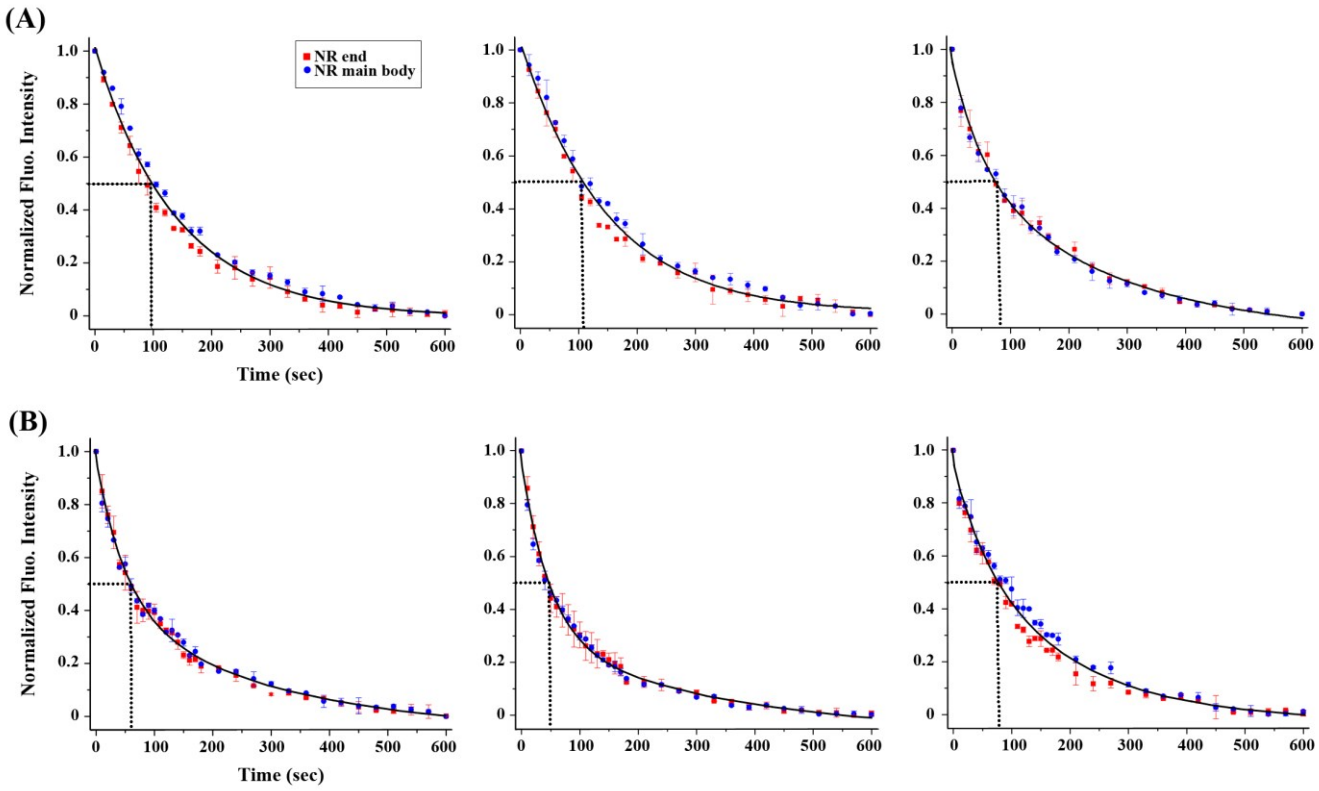

Figure 4. Photostability curves of **(A)** PT32 and **(B)** PT44 on individual ZnO NRs display the typical fluorescence decay profiles under constant illumination with the excitation wavelength. From left to right, the three photostability panels are obtained from three representative NRs of 2.5 μm, 5.5 μm, and

7.5 μm in length. Fluorescence intensity values from each PT run were normalized with respect to the highest and lowest values measured over time from the PT on the ZnO NR. Red square and blue circle data correspond to the normalized fluorescence intensity of the two PT fragments bound on the end and side facets of the single ZnO NRs, respectively. Error bars were calculated from the standard deviation values of fluorescence intensity taken from multiple points on the NR end and side facets. The solid black line corresponding to the average fluorescence intensity values measured on the NR end and side was inserted as a guide to the eye. The dotted lines mark the time for the collected signal to decrease to 50% of the initial intensity at T = 0 s.

Statistical Analysis of the Occurrence, Magnitude, and Degree of *FINE*. We further carried out statistical measurements to substantiate the occurrence, magnitude, and degree of the PT fluorescence intensity from different positions along individual NRs for over 100 ZnO NRs per each PT case and confirmed the aforementioned trends in the spatial and temporal fluorescence data summarized by several representative NR cases with facet-dependent PT adsorption. We find statistically that ZnO NRs exhibit highly intensified fluorescence signal localized on the NR ends, regardless of the intrinsic adsorption preference of PT32 and PT44. For a total of over 200 ZnO NRs assayed that exhibit variations in physical dimensions, the mean signal collected from the NR end facets is consistently considerably higher than that collected from the NR main body for both PT32 and PT44. Distributions in the biomolecular fluorescence intensities measured at T = 0 s from the NR end (left panels) and NR main body (right panels) are provided in Fig. 5 as histograms for (A) PT32 and (B) PT44. Average PT fluorescence intensities measured from the NR ends and main body are shown in the left and right panels of Fig. 5, respectively. The mean fluorescence intensity (and standard error) values obtained from the curve fits of the histograms that correspond to the measurement combinations of NR end/PT32, NR main body/PT32, NR end/PT44, the NR main body/PT44 are 5605 (132), 4399 (98), 4894 (100), and 3870 (61), respectively. When comparing the average signal collected from the NR end facet

between the adsorption cases of PT32 and PT44, PT32 is shown to have the higher mean intensity on the NR end facets. In addition, relative to the main body mean signal measured from PT44, PT32 provides the higher mean signal along the NR main body. Therefore, the similarities and differences between PT32 and PT44 in the signal distributions and intensity changes of the PT fluorescence along various positions of the NRs are also statistically validated.

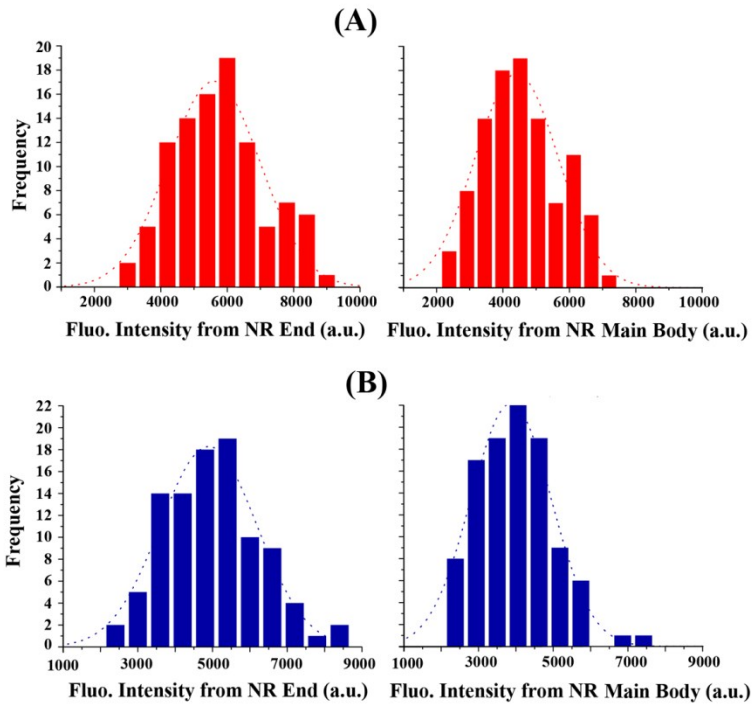

Figure 5. The intensity values on both the end and side facets of individual ZnO NRs facets are presented as histograms by examining the resulting fluorescence intensities from the adsorption cases of **(A)** PT32 and **(B)** PT44. For the statistical analysis, over 100 ZnO NRs were measured for each PT adsorption case.

PT32 versus PT44 on the NR Length-Dependent Degree of *FINE*. We then evaluated the influence of the NR physical dimensions on the degrees of signal enhancement at the NR ends in *FINE* for each

peptide case. The degree of intensification, $\Delta \boldsymbol{I}$, is defined using the average intensities collected from multiple positions on the end and side facets according to: $\Delta \boldsymbol{I} = (\boldsymbol{I}_{avg,end} - \boldsymbol{I}_{avg,middle}) / \boldsymbol{I}_{avg,middle}$. Therefore, this degree of *FINE* serves as a gauging tool for the enhancement factor of the fluorescence intensity collected from the NR end facets in reference to the NR side facets. The degree of *FINE* plot in Fig. 6 exhibits a dependence on NR length for each peptide case. The comparison graphs presented in Fig. 6 confirm that PT32 exhibits a more significant dependence of the degree of *FINE* on NR length relative to PT44. In the case of PT32, a strong linear dependence between the degree of *FINE* and NR length is found as seen in Fig. 6(A). As NR length becomes longer, the degree of *FINE* for PT32 rises from a factor of 0.1 to 0.5. For this case of PT32, increasing the NR length results in a higher amount of biomolecules adsorbed along the NR main body due to a larger surface footprint of the NR side facet. However, the surface density of the biomolecules effectively stays the same, yielding minimal changes in the average signal collected from the NR main body, $\boldsymbol{I}_{middle}$. At the same time, the average signal measured at the NR end facet, $\boldsymbol{I}_{end}$, increases significantly as shown earlier in Fig. 2(A) as the NR length increases, which subsequently escalates the degree of signal intensification, $\Delta \boldsymbol{I}$.

In contrast, for the case of PT44, the degree of *FINE* correlates weakly with NR length as shown in Fig. 6(B). With the increase in the NR length, the enhancement factor only changes from 0.1 to 0.2 for PT44. The elongations in NR length do not affect the number of end facet-preferring biomolecules and, accordingly, do not affect the degree of *FINE* significantly. For both peptides, varying NR widths showed no correlation to the degree of *FINE* for the hundreds of NRs we tested. Since increases in the diameter of the NR basal plane is anticipated to provide larger surface areas for PT44's preferential adsorption, the lack of clear correlation of NR width and the degree of *FINE* also supports that *FINE* is not derived simply from higher amounts of bimolecular adsorption at the basal plane. The aspect ratios (length:width) of the typical NRs examined under our study lie between 10:1 and 30:1. Hence, we note that such differences of the NR length-dependencies in the degree of *FINE* between the two PT adsorption cases are experimentally validated in this aspect ratio range.

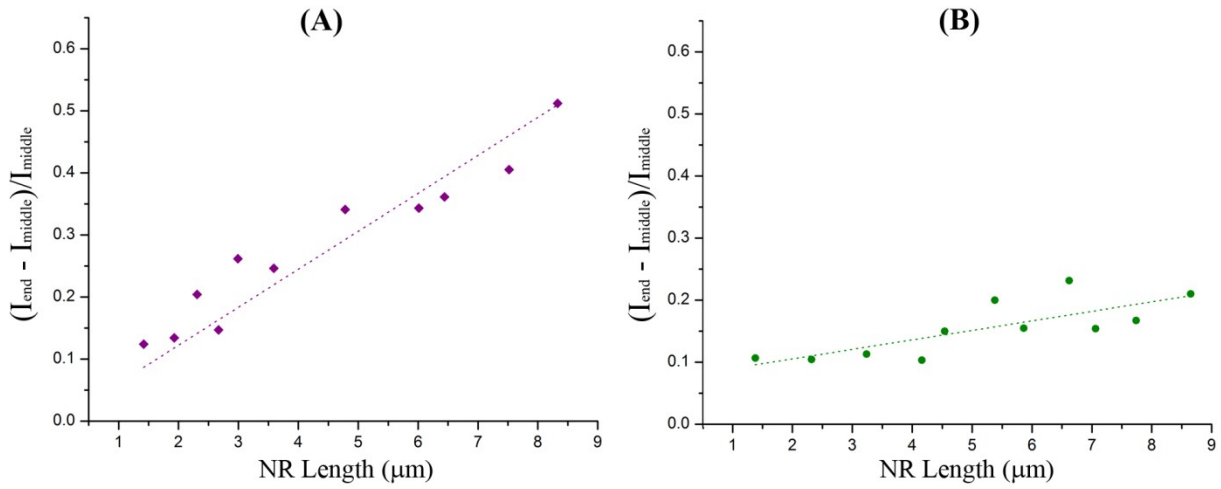

Figure 6. The varying degrees of *FINE* were evaluated with respect to the ZnO NR length for the two PT adsorption cases of **(A)** PT32 and **(B)** PT44. Similar to what we have previously reported on the degree of *FINE* measured using fluorophore-coupled proteins bound on all exposed ZnO NR facets, the degree of *FINE* from the PT32 fragments adsorbed preferentially on the NR main body exhibits a linear dependence on the NR length. On the other hand, the degree of FINE for the PT44 case with its exclusive adsorption to the NR ends shows a very weak correlation with the NR length.

FDTD Simulation Outcomes and Comparison to Experimental Findings. In order to gain a better understanding of our experimental observations, the PT-coupled ZnO NR systems of various physical dimensions were simulated via FDTD, and far-field (FF) radiation patterns were obtained for each case. The resulting FDTD data from a 517 nm-emitting electric dipole polarized perpendicular to the NR long axis and located on the side facet of a ZnO NR with a gap distance of 2 nm are displayed in Fig. 7, simulating for the PT32 case. The evaluated NR lengths are (A) 2.5 μm, (B) 5 μm, (C) 7 μm and (D) 10 μm for the same NR diameter of 100 nm. A pair of FF electromagnetic patterns is shown in Figs. 7(A)

through 7(D) for each NR with different view angles. The top patterns correspond to the spatial electromagnetic distributions observed from a monitoring plane parallel to the NR facet containing the dipole. The bottom views are the same 3D patterns with a rotation of 45°. The FF patterns in Fig. 7 show overall a symmetrically elongated shape along the long axis of the ZnO NR. The two prominent ends of the patterns with high intensity correspond to the electromagnetic power radiated along the direction parallel to the ZnO NR long axis, while the narrow waists correspond to the power radiated along the direction perpendicular to the NR. The highly elongated FF patterns indicate that most emission from the dipole is coupled into and guided by the ZnO NR, before finally being radiated out from the NR ends. When comparing the results between the NR cases of varying lengths, the longer NRs exhibit FF patterns with higher NR end intensities than the shorter ones. The outcomes further suggest that, for longer NRs, more effective directional emission behavior, coupled with a stronger waveguiding effect along the NR long axis, is anticipated as was the case for the experimental results from PT32.

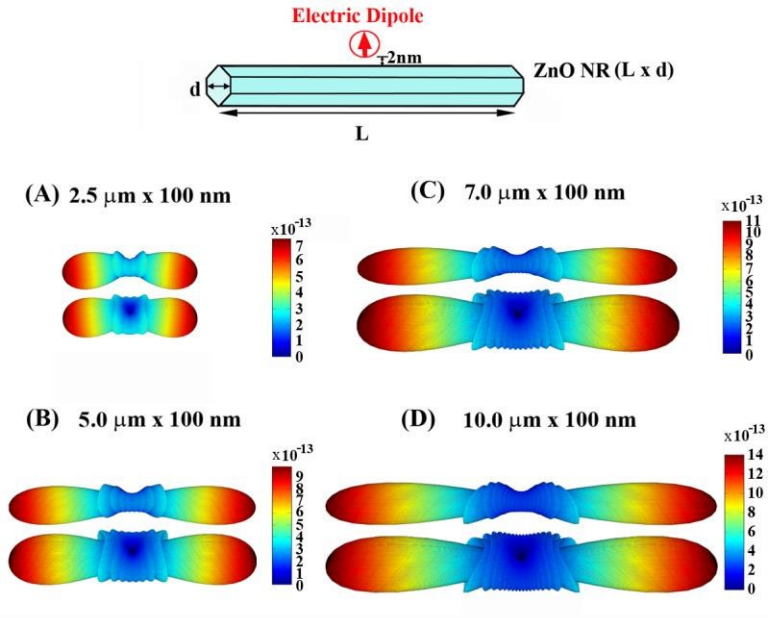

Figure 7. FDTD simulation results display the far-field patterns of the ZnO NR with the specified physical dimensions of the length (L) and diameter (d), when an electric dipole is located on the side facet similar to the PT32 case. The paired images shown for each NR case are views from different angles. The dipole emitting at 517 nm was placed 2 nm away from the prismic surface in the middle of the NR long axis. The diameter of all simulated NR cases was kept constant as 100 nm, while varying the length to (A) 2.5 μm, (B) 5 μm, (C) 7 μm, and (D) 10 μm.

Fig. 8 shows the FDTD results obtained when the same electric dipole is located at one end of the ZnO NR with a gap distance of 2 nm, corresponding to the PT44 case. The shapes of the FF patterns become asymmetric along the direction parallel with the NR long axis. Simulations were performed by modelling ZnO NRs of the same physical dimensions as in the FDTD evaluations of Fig. 7, and the resulting data are presented in a pair of FF electromagnetic patterns shown in Figs. 8(A) through 8(D). As illustrated in Fig. 8, the FF patterns still exhibit NR-mediated guiding of the electromagnetic radiation after the dipole emission is coupled into ZnO NR from one end. However, the radiation characteristics into the far field are different than the earlier case. The directional emission behavior is pronounced only on the opposite NR end to the location of initial emission coupling, whose effect shows only a slight increase with longer NRs.

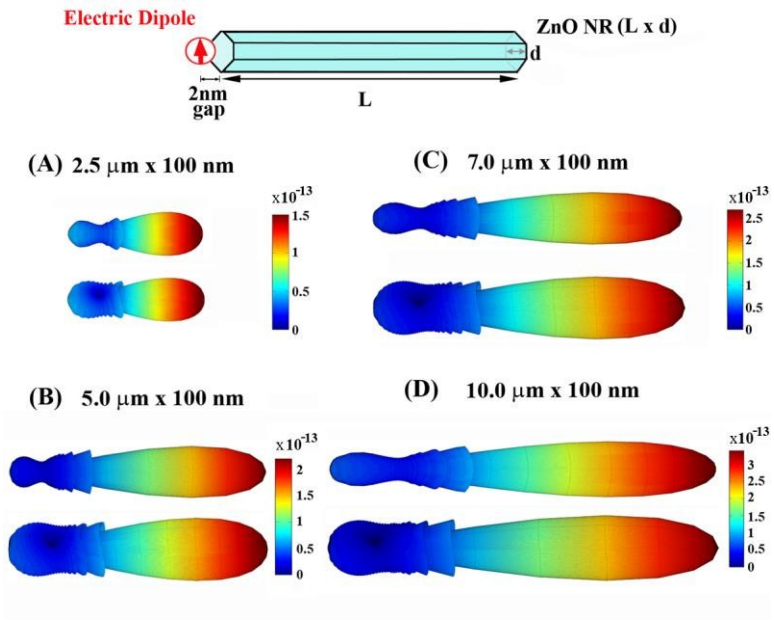

Figure 8. The FDTD calculated patterns show the far-field radiation distributions of ZnO NRs with the specified physical dimensions of the length (L) and diameter (d) when an electric dipole is located on the end facet. The paired images shown for each NR case are views from different angles. Modelling the PT44 case, the dipole emitting at 517 nm was placed on top of the basal plane, 2 nm away from the surface. The diameter of all simulated NR cases was kept constant as 100 nm, while varying the length to (A) 2.5 μm, (B) 5 μm, (C) 7 μm, and (D) 10 μm.

From the FDTD simulation results presented in Figs. 7 and 8, we found that the position of the electric dipole determines the general shape of the FF pattern for a given radiation wavelength, while the length of the ZnO NR determines how directionally the electromagnetic power can radiate to the far field. Furthermore, we qualitatively estimated the degree of *FINE* from the simulated FF patterns and correlated the simulation outcomes to the experimental results discussed earlier. The intensity values at the waist and at the end of the FF patterns, corresponding to the electromagnetic power radiated perpendicular and parallel to the NR long axis, were first determined as $\boldsymbol{I}_{middle}$ and $\boldsymbol{I}_{end}$, respectively. We then calculated the degree of *FINE* by $(\boldsymbol{I}_{end} - \boldsymbol{I}_{middle}) / \boldsymbol{I}_{middle}$ for both simulation cases shown in Figs. 7 and 8, and plotted the results as a function of the NR length, as displayed in Fig. 9. When the dipole is

placed on the side facet, the degree of *FINE* is largely proportional to and sensitive to the NR length, as shown in Fig. 9(A). On the contrary, when the dipole is placed on the end facet, the degree of *FINE* stays flatter and its dependence on the NR length is relatively weak, as seen in Fig. 9(B). The plots directly comparing the outcomes between the experiments and FDTD simulations are displayed in Fig. 9(C) and 9(D) for the two cases of PT32 and PT44, respectively. The trends from the simulation outcomes for the middle (Fig. 9, case (A)) and end (Fig. 9, case (B)) dipole cases agree very well with the experimental observations from PT32 and PT44 in terms of the influence of the NR length on the degree of *FINE*.

Additional work is in progress to understand further the effects of varying excitation light, fluorophore, and PT concentration conditions on the presence and degree of *FINE* as well as to examine far- and near-field electric field distributions along individual NRs through computer simulation means while considering multiple dipole adsorption scenarios.

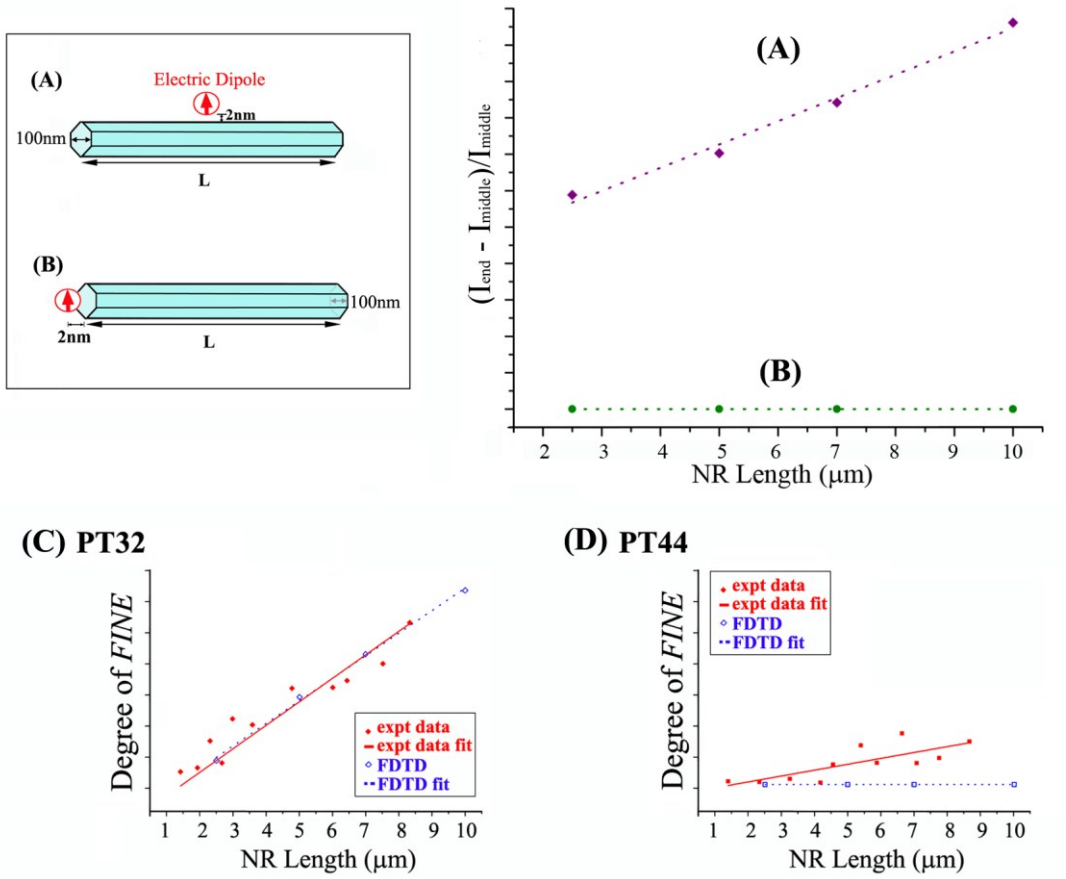

Figure 9. (A and B) The dependence of the degree of *FINE* on the ZnO NR length is estimated from the FDTD calculated intensity values of the FF simulations. Data shown in (A) and (B) are obtained from ZnO NRs of different lengths when a dipole is placed **(A)** on the prismic and **(B)** on the basal plane of the NR, modeling the two cases of PT32 and PT44 in the experiments, respectively. **(C and D)** The experimental and computer simulation results are compared in a single graph for the **(C)** PT32 and **(D)** PT44 case. The solid and open symbols correspond to the experimental data and FDTD simulation outcomes, respectively. The solid and dashed lines are the respective linear fits through the data from the experiment and the FDTD simulations, respectively.

SUMMARY

In summary, we have investigated the role by which NR facet-selective biomolecular adsorption affects the fluorescence intensification profiles of single ZnO NR platforms by employing fluorophore-tagged peptides exhibiting contrasting binding preferences for different crystallographic planes of ZnO. Specifically, we employed PT32 and PT44 which are known to preferentially bind to the exposed prismic planes along the ZnO NR main body and the basal planes located at the NR ends, respectively. The resulting biomolecular fluorescence profiles of each peptide's discriminatory adsorption on individual ZnO NRs were characterized experimentally and simultaneously probed using FDTD simulations. Similarities and differences in the spatial and temporal fluorescence characteristics measured along single NRs between the crystalline NR facet-specific versus -nonspecific biomolecular adsorption scenarios were further revealed.

The phenomenon of *FINE* was persistently observed on the individual ZnO NR platforms, irrespective of the favored crystallographic locations for peptide adsorption. However, the inherent discrimination of each peptide towards particular ZnO facets was found to notably affect the degree, intensity, and temporal stability of the biomolecular fluorescence signal. For the prismic facet-bound peptide case (PT32), the intensity and photostability of the bimolecular emission was found to be higher relative to the case of preferred adsorption at the NR basal planes (PT44). Further, the predilection of PT32 to favor binding along the NR main body produced a stronger correlation between the degree of *FINE* and the NR length in comparison with the end facet-binding scenario of PT44. When compared to the previous nondiscriminatory adsorption circumstances exhibiting much prolonged photostability on the NR basal relative to the prismic planes, the time-dependent decay profiles of the fluorescence signal examined spatially along the NR for the preferential binding cases displayed negligible differences between the NR basal and prismic planes.

The FDTD simulations substantiated the experimental trends in the occurrence, magnitude, and degree of *FINE* for each discriminatory peptide-binding scenario and further provided a basis to evaluate the complex origins of our experimental observations for the two PT cases. Such understandings are

anticipated to further the processing and interpretation of the fluorescence signal from various ZnO NR biosensors, especially for those fabricated by engineering site-directed biomolecular adsorption to ZnO NRs. Therefore, our findings in this study will be highly beneficial in promoting the development of innovative probe and sensor applications exploiting the ability to spatially localize biomolecules on specific areas of ZnO NRs in addition to utilizing the directionally guided and locally enhanced optical signal enabled by ZnO NRs.

ACKNOWLEDGEMENTS

The authors acknowledge financial support on this work by the National Institutes of Health, National Research Service Award (1R01DK088016) from the National Institute of Diabetes and Digestive and Kidney Diseases.

References

1. A. B. Dahlin, *Sensors*, 2012, **12**, 3018-3036.
2. S. Lindström and H. Andersson-Svahn, *Biochim. Biophys. Acta* 2011, **1810**, 308-316.
3. S. Vaddiraju, I. Tomazos, D. J. Burgess, F. C. Jain and F. Papadimitrakopoulos, *Biosens. Bioelectron.*, 2010, **25**, 1553-1565.
4. M. R. Melo, S. Clark and D. Barrio, *Clin. Chem. Lab. Med.*, 2011, **49**, 581-586.
5. V. Adalsteinsson, O. Parajuli, S. Kepics, A. Gupta, W. B. Reeves and J. Hahm, *Anal. Chem.*, 2008, **80**, 6594-6601
6. A. Dorfman, N. Kumar and J. Hahm, *Adv. Mater.*, 2006, **18**, 2685-2690.
7. A. Dorfman, N. Kumar and J. Hahm, *Langmuir*, 2006, **22**, 4890-4895.
8. A. Dorfman, O. Parajuli, N. Kumar and J. Hahm, *J. Nanosci. Nanotech.*, 2008, **8**, 410-415.
9. N. Kumar, A. Dorfman and J. Hahm, *Nanotech.*, 2006, **17**, 2875-2881.
10. J. Bao, M. A. Zimmler, F. Capasso, X. Wang and Z. F. Ren, *Nano Lett.*, 2006, **6**, 1719-1722.
11. M. Willander, O. Nur, Q. X. Zhao, L. L. Yang, M. Lorenz, B. Q. Cao, J. Z. Pérez, C. Czekalla, G. Zimmermann, M. Grundmann, A. Bakin, A. Behrends, M. Al-Suleiman, A. El-Shaer, A. C. Mofor, B. Postels, A. Waag, N. Boukos, A. Travlos, H. S. Kwack, J. Guinard and D. L. S. Dang, *Nanotechnology*, 2009, **20**, 332001.
12. C. X. Xu and X. W. Sun, *Appl. Phys. Lett.*, 2003, **83**, 3806-3808.
13. Y. K. Tseng, C. J. Huang, H. M. Cheng, I. N. Lin, K. S. Liu and I. C. Chen, *Adv. Funct. Mater.*, 2003, **13**, 811-814.
14. M. H. Huang, S. Mao, H. Feick, H. Q. Yan, Y. Y. Wu, H. Kind, E. Weber, R. Russo and P. D. Yang, *Science*, 2001, **292**, 1897-1899.
15. J. C. Johnson, H. Yan, R. D. Schaller, L. H. Haber, R. J. Saykally and P. Yang, *J. Phys. Chem. B*, 2001, **105**, 11387-11390.
16. C. Zhang, F. Zhang, T. Xia, N. Kumar, J.-i. Hahm, J. Liu, Z. L. Wang and J. Xu, *Opt. Express*, 2009, **17**, 7893-7900.

17. J. C. Johnson, H. Yan, H.-J. Choi, K. P. Knutsen, P. B. Petersen, M. Law, P. Yang and R. J. Saykally, *Proc. SPIE* 2010, **5223**, 187-196.

18. J. C. Johnson, H. Yan, P. Yang and R. J. Saykally, *J. Phys. Chem. B*, 2003, **107**, 8816-8828.

19. T. Voss, G. T. Svacha, E. Mazur, S. Müller, C. Ronning, D. Konjhodzic and F. Marlow, *Nano Lett.*, 2007, **7**, 3675-3680.

20. R. Yan, D. Gargas and P. Yang, *Nature Photonics* 2009, **3**, 569-576.

21. W. Hu, Y. Liu, T. Chen, Y. Liu and C. M. Li, *Adv. Mater.*, 2015, **27**, 181-185.

22. A. V. Kachynski, A. N. Kuzmin, M. Nyk, I. Roy and P. N. Prasad, *J. Phys. Chem. C*, 2008, **112**, 10721-10724.

23. Y. Liu, K. Ai, Q. Yuan and L. Lu, *Biomaterials*, 2011, **32**, 1185-1192.

24. Y. Yin, Y. Sun, M. Yu, X. Liu, T. Jiang, B. Yang, D. Liu, S. Liu and W. Cao, *Sci. Rep.*, 2015, **5**.

25. J. Zhao, D. Wu and J. Zhi, *Bioelectrochem.*, 2009, **75**, 44-49.

26. M. Singh, R. Jiang, H. Coia, D. S. Choi, A. Alabanza, J. Y. Chang, J. Wang and J.-i. Hahm, *Nanoscale*, 2015, **7**, 1424-1436.

27. M. Singh, S. Song and J.-i. Hahm, *Nanoscale*, 2014, **6**, 308-315.

28. A. Vallee, V. Humblot and C.-M. Pradier, *Acc. Chem. Res.*, 2010, **43**, 1297-1306.

29. M. Bachmann, K. Goede, A. G. Beck-Sickinger, M. Grundmann, A. Irbäck and W. Janke, *Angew. Chem. Int. Ed.*, 2010, **49**, 9530-9533.

30. D. Rothenstein, B. Claasen, B. Omiecienski, P. Lammel and J. Bill, *J. Am. Chem. Soc.*, 2012, **134**, 12547-12556.

31. J. Baier, N. J. Blumenstein, J. Preusker, L. P. H. Jeurgens, U. Welzel, T. A. Do, J. Pleiss and J. Bill, *CrystEngComm*, 2014, **16**, 5301-5307.

32. M. M. Tomczak, M. K. Gupta, L. F. Drummy, S. M. Rozenzhak and R. R. Naik, *Acta Biomater.*, 2009, **5**, 876-882.

33. M.-K. Liang, O. Deschaume, S. V. Patwardhan and C. C. Perry, *J. Mater. Chem.*, 2011, **21**, 80-89.

34. A. Merzlyak and S.-W. Lee, *Curr. Opin. Chem. Bio.*, 2006, **10**, 246-252.

35. W. L. Bond, *J. Appl. Phys.*, 1965, **36**, 1674-1677.

36. X. Gao, L. Yang, J. A. Petros, F. F. Marshall, J. W. Simons and S. Nie, *Curr. Opin. Biotechnol.*, 2005, **16**, 63-72.

37. X. X. Han, Y. Kitahama, Y. Tanaka, J. Guo, W. Q. Xu, B. Zhao and Y. Ozaki, *Anal. Chem.*, 2008, **80**, 6567-6572.

38. A. Margineanu, J. Hofkens, M. Cotlet, S. Habuchi, A. Stefan, J. Qu, C. Kohl, K. Müllen, J. Vercammen, Y. Engelborghs, T. Gensch and F. C. De Schryver, *J. Phys. Chem. B*, 2004, **108**, 12242-12251.

39. L. Song, E. J. Hennink, T. Young and H. J. Tanke, *Biophys. J.*, 1995, **68**, 2588-2600.

Graphical Abstract